Monthly Notices of the ROYAL ASTRONOMICAL SOCIETY

MNRAS **539,** 3732–3740 (2025) https://doi.org/10.1093/mnras/staf729
Advance Access publication 2025 May 2

ExoMol photodissociation cross-sections – II. Continuum absorption and pre-dissociation spectra for the hydroxyl radical

Georgi B. Mitev, Marco Pezzella, Charles A. Bowesman, Jingxin Zhang, Sergei N. Yurchenko and Jonathan Tennyson ★

Department of Physics and Astronomy, University College London, Gower St, London WC1E 6BT, UK

Accepted 2025 May 1. Received 2025 April 30; in original form 2025 March 16

ABSTRACT

The photodissociation of hydroxyl has seen much theoretical study and temperature-independent photodissociation cross-sections are available in the Leiden photodissociation and photoionization data base. Such cross-sections are important for calculations in UV rich environments, concerning not only abundances of hydroxyl but other hydrogen and oxygen containing species, notably water. Temperature-dependent photodissociation cross-sections comprised of smoothed transitions to continuum levels of the A $^2\Sigma^+$, B $^2\Sigma^+$, 1 $^2\Delta$, and 1 $^2\Sigma^-$ electronic states and appropriately broadened pre-dissociative states of A $^2\Sigma^+$, B $^2\Sigma^+$, and C $^2\Sigma^+$ are calculated. These are produced using the same model as the ExoMol OH line list, MYTHOS and cover the temperature range of $T \in [100, 200, ..., 8000]$ K each with a grid spacing of 0.1 nm from 82.8 to 2000 nm. Compared to the data presented by Leiden we find increased photodissociation at long wavelengths due to pre-dissociation and strong temperature dependence of the photodissociation rates. The OH MYTHOS photodissociation cross-sections and results as a function of temperature are available for download via www.exomol.com and are also available in a form suitable for study of non-local thermodynamic equilibrium effects.

Key words: molecular data – Earth – exoplanets – planets and satellites: atmospheres.

1 INTRODUCTION

This paper is the third in a series on the hydroxyl radical. In Mitev, Yurchenko & Tennyson (2024), henceforth referred to as Paper I, the spin-orbit pre-dissociation lifetimes of the A $^2\Sigma^+$ state of OH are calculated using a modified stabilization method. Mitev et al. (2025) (henceforth referred to as Paper II) introduces the MYTHOS data set, containing bound–bound transitions in the form of a line list of .STATES and .TRANS files, and bound-continuum transitions from X $^2\Pi$ to continuum states of A $^2\Sigma^+$, B $^2\Sigma^+$, 1 $^2\Sigma^-$, and 1 $^2\Delta$ in the form of .CONT files.

Paper I studies pre-dissociation, whereby the molecule dissociates through the non-radiative decay from a bound electronic state to a repulsive electronic state. When pre-dissociation is considered, bound to bound transitions where the upper state is pre-dissociative have an increased lifetime broadening parameter. An example of such transitions are those in the $A\ ^2\Sigma^+ \leftarrow X\ ^2\Pi$ band system in OH where lifetime broadening can be as big as 3 cm^{-1}. Pre-dissociation, as it is a dissociative process, is a constituent in the temperature-dependent photodissociation cross-sections discussed in this paper. The other process that needs to be considered is direct photodissociation, which will simply be referred to as photodissociation hereafter. This process is distinct from pre-dissociation as this is due to a transition from a bound electronic state directly to the continuum, a one-step process. Pre-dissociation on the other hand is a two-step process, going from bound → (quasi-)bound → continuum.

Photodissociation is an important marker not only of the abundance of photofragments like excited oxygen, but also as a marker for other hydroxyl containing molecules such as water (Dalgarno 1987; Wang et al. 2017; Schoerghofer et al. 2021; Tang et al. 2021; Tabone, van Dishoeck & Black 2024). Water can be formed efficiently at high temperatures through the reaction between the hydroxyl radical and molecular hydrogen ($OH + H_2 \rightleftharpoons H_2O + H$). Moreover, in the presence of UV radiation, water photodissociates and forms OH ($H_2O + \gamma_{UV} \rightarrow OH + H$) (Wampfler et al. 2010; Yuan, Dixon & Yang 2011). Laboratory studies also show that photodissociation of water can lead to highly excited OH radicals (Czarny, Felenbok & Lefebvre-Brion 1971; Harich, Yang & Yang 2001; Cheng et al. 2011; Dixon et al. 2013; Heays et al. 2018; Chang et al. 2019, 2020a) leading to observable emissions from both astronomical objects (Zhu & Yee 2007; Tappe et al. 2008; Carr & Najita 2014; Chang et al. 2020b; Parkinson et al. 2021; Tabone et al. 2021) and the night sky (Meinel 1950); this also leads to the need to treat non-local thermodynamic equilibrium (non-LTE) effects in OH. Spectral features resulting from photodissociation are very broad, absorbant, and heavily temperature dependent at longer wavelengths. Modelling the photochemistry of hot planetary and stellar environments requires a description of temperature-dependent photodissociation cross sections.

OH direct photodissociation has several channels. Transitions from the ground state to the 1 $^2\Sigma^-$ and 1 $^2\Delta$ electronic states and continuum states of A $^2\Sigma^+$ and B $^2\Sigma^+$ results in photodissociation

★ E-mail: j.tennyson@ucl.ac.uk

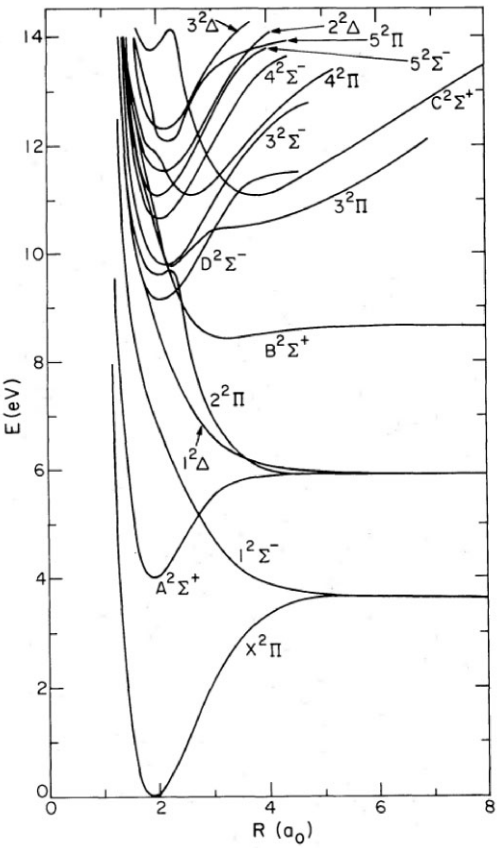

Figure 1. *Ab initio* doublet potential energy curves of OH reproduced from van Dishoeck & Dalgarno (1984b) with permission.

(van Dishoeck & Dalgarno 1983; Nee & Lee 1984a; Kurucz, van Dishoeck & Tarafdar 1987; Radenović et al. 2008; Li & Zhang 2011). The B $^2\Sigma^+$ state has a shallow bound region with a well depth of around 2000 cm^{-1}; this region is modelled as such and is included in the MYTHOS line list as described in Paper II. In general, however, all transitions to the B $^2\Sigma^+$ state are dissociative due to crossings with the local 2 $^2\Pi$ repulsive state resulting in pre-dissociation (van Dishoeck & Dalgarno 1984a, 1984b; Sun et al. 2020). Hwang et al. (2001) found experimentally that the total lifetimes of the $v = 0$ band of B $^2\Sigma^+$ are on the order of 100 ns for $J = 0.5$ decreasing exponentially to 10 ns for $J = 4.5$, which they claim agree well with Sappey, Crosley & Copeland (1989). These data are not available however, and are only given as plots, so making use of them is difficult. This pre-dissociative effect has not been considered explicitly in this study.

OH can also directly photodissociate through the 2 $^2\Pi$ state (Kalyanaraman & Sathyamurthy 1994). van Dishoeck & Dalgarno (1983) and van Dishoeck et al. (1984) calculated *ab initio* photodissociation cross-sections for transitions from X $^2\Pi$ to 1 $^2\Sigma^-$, 1 $^2\Delta$, B $^2\Sigma^+$, and 2 $^2\Pi$ states. The photodissociation cross-section for 2 $^2\Pi \leftarrow$ X $^2\Pi$ is centred around ∼95 000 cm^{-1} and is considerably narrower than the other cross-sections due to narrowness of the upper state potential energy curve. Furthermore, there is more than this direct photodissociation cross-section in this region involving the 2 $^2\Pi$ state. van Dishoeck & Dalgarno (1984b) give a nice visualization of the many potential energy curves of OH including high energy ion-pair states, such as the C $^2\Sigma^+$ state, and Rydberg states, which is reproduced here as Fig. 1. This figure shows that the 2 $^2\Pi$ state has a significant avoided crossing with the 3 $^2\Pi$ state. If one is to diabatise (Brady et al. 2024) these curves to remove this crossing, we find that the minimum of the 3 $^2\Pi$ state lies around the equilibrium geometry of X $^2\Pi$, meaning the Franck-Condon overlap in this region is strong. van Dishoeck et al. (1984) showed that the photodissociation cross-section of 2 $^2\Pi$ is strongly affected by the presence of the 3 $^2\Pi$ state. The 3 $^2\Pi$ state pre-dissociates through the 2 $^2\Pi$ state, meaning that effective modelling of the 2 $^2\Pi$ photodissociation cross-section would also require modelling the 3 $^2\Pi$ pre-dissociation. At this stage, this has not been attempted.

The Leiden data base (Hrodmarsson & van Dishoeck 2023) contains photodissociation cross-sections for OH, based on the calculations of van Dishoeck & Dalgarno (1983, 1984b, a) and van Dishoeck et al. (1984). These cross-sections will be used for comparison in Section 3.

Within the ExoMol project, studying the temperature dependence of photodissociation cross-sections started with the work of Pezzella, Yurchenko & Tennyson (2021, 2022), where cross-sections for HCl, HF, NaCl, and BeH$^+$ were computed for temperatures up to 10 000 K. This study on diatomics made use of both a modification of the stabilization method (which was also used to study pre-dissociation in Paper I) and an implementation of Gaussian smoothing, whereby a Gaussian line profile with a constant Half-Width at Half-Maximum (HWHM) $= \alpha$ is applied to the cross-section to smooth the discretized continuum cross-section while maintaining the integral value, hence, the rates. Using the stabilization method to compute photodissociation cross-sections is prohibitively expensive, so for larger molecules, this smoothing procedure is necessary and has recently been applied to HCN (Pezzella et al. 2024).

In this paper, the temperature-dependent photodissociation cross-sections for the X $^2\Pi \rightarrow$ (A $^2\Sigma^+$, B $^2\Sigma^+$, 1 $^2\Sigma^-$, 1 $^2\Delta$) continuum absorption transitions are calculated. This is done by adapting the Gaussian smoothing method of Pezzella et al. (2021). This adaptation is distinct from the root-finding approach in Pezzella et al. (2024) and applies the particle-in-a-box approximation to predict transition spacings, this is dubbed energy-dependent smoothing (EDS). The root-dependent smoothing (RDS) and EDS approaches are discussed and compared in Section 2. Final results of this implementation is presented in Section 3 along with a summary of constituent transitions in this data set. Conclusions and discussions on future work are given in Section 4.

2 METHODS

2.1 Leveraging DUO spectroscopic models

As with the treatment of pre-dissociation lifetimes in Paper I, we leverage the DUO spectroscopic model constructed in Paper II. Starting with this model, one can compute an absorption cross-section using EXOCROSS (Yurchenko, Al-Refaie & Tennyson 2018) or PYEXOCROSS (Zhang, Tennyson & Yurchenko 2024). As discussed earlier, modelling the continuum with a bound-state-like solution as is implemented in DUO results in a discretization of the continuum energy levels. This contradicts the infinite number of states expected for dissociative electronic states and results in a concentration of the absorption cross-section in finite regions.

The method which was applied by Pezzella et al. (2021, 2022) to remedy this is to distribute discretized transition intensities over the continuous spectral region using a normalized Gaussian profile. The

form of the Gaussian distribution is given by

$$G(\tilde{\nu};\tilde{\nu}_0,\alpha)=\sqrt{\frac{\ln 2}{\pi}}\alpha^{-1}\exp-\frac{(\tilde{\nu}-\tilde{\nu}_0)^2\ln 2}{\alpha^2}, \quad (1)$$

where $\tilde{\nu}$ is the wavenumber in cm^{-1}, $\tilde{\nu}_0$ is the line position in cm^{-1}, and α is Gaussian HWHM. Applying this filter to the discretized spectra has the effect of lowering the maximal intensity and *smoothing* the cross-section into continuum while maintaining the integral value and, indeed, photodissociation rates (Pezzella et al. 2021).

The photodissociation rate, k, of a molecule at temperature, T, dissociated by a field with flux, $F(\lambda)$ between the wavelengths λ_1 and λ_2, is given by

$$k(T)=\int_{\lambda_1}^{\lambda_2}F(\lambda)\sigma(\lambda;T)\mathrm{d}\lambda, \quad (2)$$

where $\lambda\propto 1/\nu$. This value, assuming that λ_1 and λ_2 cover the full range of the calculated cross-section, remain the same whether or not the cross-section is smoothed (Pezzella et al. 2021).

The Gaussian smoothing method was further developed by Pezzella et al. (2024), where criteria for optimal values of α are proposed along with an automated procedure to implement them. While this method is effective and is likely the only viable option for polyatomic molecules with huge numbers of transitions, for diatomic molecules, a further optimization can be made and is discussed in Section 2.2.

2.2 Energy-dependent smoothing

One of the shortcomings of Gaussian smoothing method is the choice of the parameter α in equation (1). As was discussed by Uhlikova et al. (2025), the optimal value is close to the distance between the discretized continuum states and proposed the 'particle-in-a-box' model. In their model, the value of α is estimated using the particle in a box quantum number. Here we extend this idea to use the separation of the (discretized) energies of a repulsive state to obtain optimal value of α as follows.

When solving for repulsive states in DUO using a discretized solver, the gaps between discretized (vibrational) states obtained increase with the excitation. Let us consider the model of the particle in a box for the repulsive state. In this case, the term values (cm^{-1}) scale as the square of its counting number n,

$$E_n=\frac{n^2h^2}{8mL^2}, \quad (3)$$

where h is Planck's constant, L is the length of the box, and m is the mass of the particle. Within DUO, the discretized solution can be associated with a 'vibrational' quantum number v assigned by counting states of increasing energies for a given pair of total angular momentum, J, and parity, τ, quantum numbers. Using v as the counting number, and the approximation above, we expect that the energy difference between vibrational levels,

$$\Delta E(v)=E_{v+1}-E_v \quad (4)$$

is approximately,

$$\Delta E(v)=k(2v+1),$$

or, in terms of energy,

$$\Delta E(E)=k\left(2\sqrt{\frac{E}{k}}+1\right), \quad (5)$$

where k is some appropriate constant, which in the case of equation (3) is given by

$$k=\frac{h^2}{8mL^2}.$$

Hence, the 'vibrational' gaps between discretized states can be expected to scale linearly with $\sqrt{E}$. Extending this to transition wavenumbers through the analogous treatment for equation (5),

$$\tilde{\nu}_{v'',v'}=E_{v'}-E_{v''} \quad (6)$$

for the the gaps between the discretized transition wavenumbers

$$\Delta\tilde{\nu}_{v'',v'}=\tilde{\nu}_{v'',v'+1}-\tilde{\nu}_{v'',v'} \quad (7)$$

we obtain

$$\Delta\tilde{\nu}_{v''}(\tilde{\nu})=a\sqrt{\tilde{\nu}}+b, \quad (8)$$

where a and b are some constants. This relationship is found to hold reasonably well, especially at higher $\tilde{\nu}$ as the potential curve of the repulsive state more closely approximates a vertical potential well as in the model of a particle in a box. Fig. 2 shows this relationship for the case of $\mathrm{X}\,^2\Pi\rightarrow 1\,^2\Delta$.

The relationship here is used to 'fill in the gaps' between neighbouring transitions as in the methods described by Pezzella et al. (2024). This method allows one to vary the Gaussian HWHM α for each transition based on the lower state vibrational level and the energy of the transition or transition wavenumber $\tilde{\nu}$,

$$\alpha(v'',\tilde{\nu})=\Delta\tilde{\nu}_{v''}(\tilde{\nu})=a\sqrt{\tilde{\nu}}+b. \quad (9)$$

Here, we consider transitions from a given vibrational state in $\mathrm{X}\,^2\Pi$ to discretized 'vibrational' states in the repulsive states, i.e.

$$|\mathrm{X}\,^2\Pi,J'',\Omega'',v''\rangle\rightarrow|\mathrm{U},J',\Omega',v'\rangle, \quad (10)$$

where U is a repulsive electronic state and Ω is the quantum number describing the projection of the total angular momentum on the molecular axis. What we are interested in here is the difference in the transition wavenumbers, $\Delta\tilde{\nu}_{v''}(\tilde{\nu})$, which is approximated by the treatment in equations (7) and (8) as given by

$$\begin{aligned}\Delta\tilde{\nu}_{v'',v'}=\;&\tilde{\nu}(|\mathrm{X}\,^2\Pi,J'',\Omega'',v''\rangle\rightarrow|\mathrm{U},J',\Omega',v'+1\rangle)\\&-\tilde{\nu}(|\mathrm{X}\,^2\Pi,J'',\Omega'',v''\rangle\rightarrow|\mathrm{U},J',\Omega',v'\rangle).\end{aligned} \quad (11)$$

In this work, we use the value of $\Delta\tilde{\nu}_{v''}(\tilde{\nu})$ as the value of the Gaussian HWHM α. Discrete transition spectra are evaluated and transitions where the $\mathrm{X}\,^2\Pi$ state $v=v''$ are grouped to evaluate $\Delta\tilde{\nu}_{v''}(\tilde{\nu})$. Fig. 2 shows an example of such dependence of $\Delta\tilde{\nu}_{v''}(\tilde{\nu})$ for $\mathrm{X}\,^2\Pi\rightarrow 1\,^2\Delta$ of OH. This is then squared (see the right panel of Fig. 2) and a linear regression model is applied to extract an analytic representation of α as the transition energy-dependent vibrational gap.

As discussed in Paper II, vibrational quantum labels are not always reliable, specially above the dissociation energy of $D_\mathrm{e}(\mathrm{X}\,^2\Pi)$; indeed the vibrational labels are only approximate in any multistate system. This has an implication on the above grouping in equation (9) which may introduce outliers thus breaking the linear relationship of $\Delta\tilde{\nu}_{v''}(\tilde{\nu}^2)$ in equation (9). Therefore a Huber loss regression algorithm (Huber & Ronchetti 2009; Bowesman et al. 2024), which is more resistant to outliers, was used in place of a least-squares regression.

For each group of transitions with distinct v'', a new regression model, with coefficients a and b, is calculated, stored, and used to produce α given that the input for the model now becomes the individual transition frequencies in the .TRANS file.

Smoothing was performed using the program PYEXOCROSS (Zhang et al. 2024) in which one can set a Gaussian HWHM for each

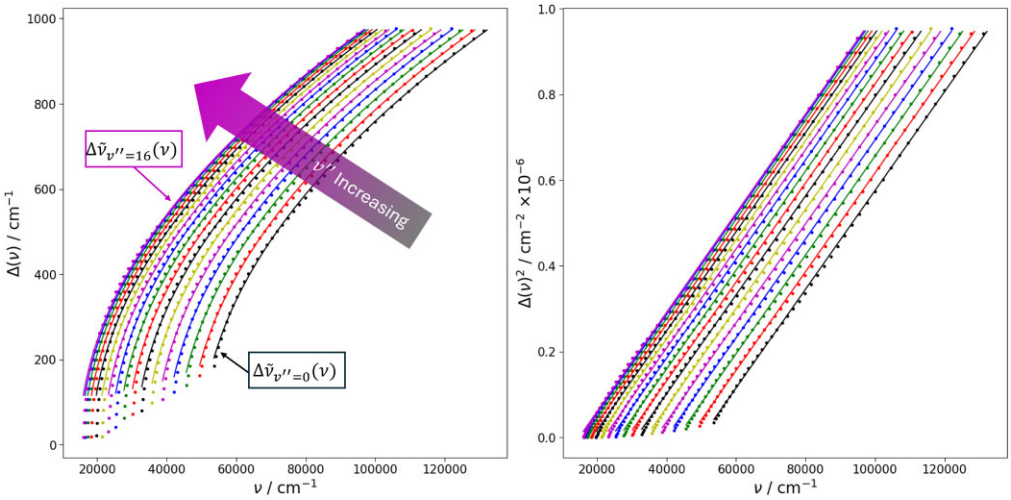

Figure 2. $\Delta\tilde{\nu}_{v''}(\tilde{\nu})$ for the set of transitions, X $^2\Pi \rightarrow 1\,^2\Delta$ of OH. Points of the same colour correspond to progressively higher v' with increasing v.

transition line by re-purposing the column in the .TRANS file corresponding to $\tilde{\nu}$ (see Tennyson et al. (2023) for a description of such data structures) to hold instead line-by-line values for α as per equation (9). Essentially, this approach approximates the transition frequency gap between transitions such as that in equation (11) by accounting for anomalous assignments in v' as discussed in Paper II, once again, 'filling in the gaps' of the discrete spectrum.

With this, one can produce photodissociation cross-sections smoothed as a function of the transition frequency. The benefits of this method is that it is simple to implement, as line-by-line line profiles are built into PYEXOCROSS. This procedure makes use of the implicit energy distribution of continuum states in the particle in a box approximation, requiring less supervision from a practitioner than do the procedures of Pezzella et al. (2021, 2022, 2024). It is likely, however, that this approach is limited to applications to diatomic molecules, as the increased degrees of freedom in polyatomic molecules make this infeasible to implement.

To compare our model of adaptive HWHM with the model of constant HWHM by Pezzella et al. (2024), Fig. 3 presents calculated cross-sections using both models. At low-to-moderate $\tilde{\nu}$, the cross-sections agree well, as $\alpha(\tilde{\nu})$ in this region is close to the value achieved with the uniform Gaussian method. At high $\tilde{\nu}$, however, we see that discrete structures remain in the top panel, whereas they are appropriately smoothed in the lower panel.

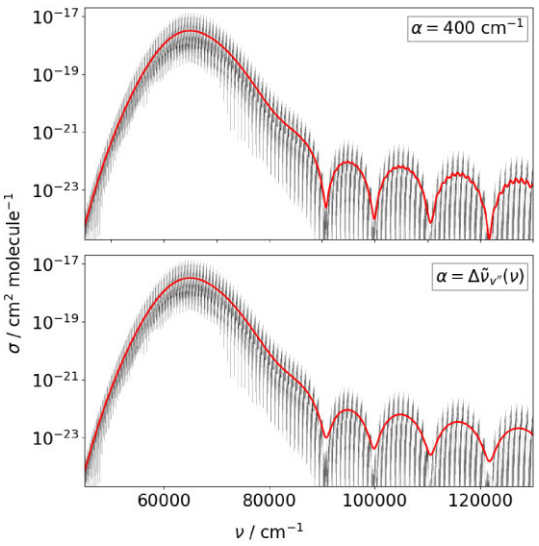

Figure 3. Photodissociation cross-section for the $1\,^2\Sigma^- \leftarrow$ X $^2\Pi$ transitions of OH with Gaussian smoothing applied for $\alpha = 400$ (top panel) and energy-dependent smoothing applied (bottom panel).

2.3 Pre-dissociative transitions

Because A $^2\Sigma^+$, B $^2\Sigma^+$, and C $^2\Sigma^+$ are lying in the continuum region of the X $^2\Pi$ states (above the first dissociation channel $D_0(X)$), the corresponding rovibronic states in A $^2\Sigma^+$, B $^2\Sigma^+$, and C $^2\Sigma^+$ are pre-dissociative, as well as the transitions to these states from the ground X $^2\Pi$ rovibronic states. These transitions are all included in the temperature-dependent photodissociation cross-sections $\sigma(\lambda, T)$, where λ is the wavelength of the photodissociating photon, produced in this paper. Individual lines are modelled using the Doppler and lifetime broadening effects by using Voigt profiles. These cross-sections are generated in a wavelength grid λ of 0.01 nm from 82.8 to 2000 nm for temperatures from 100 to 10 000 K with a step of 100 K in line with previous cross-sections (Pezzella et al. 2022); as is usual for photodissociation cross-sections, zero pressure was assumed. Pre-dissociation broadening for the A $^2\Sigma^+$ state due to the interactions with the repulsive state $1\,^2\Sigma^-$ is accounted for explicitly as given in Papers I and II by convoluting the pre-dissociation lifetime, τ_p, with the radiative lifetime, τ_{rad}, to produce the total lifetime,

$$\tau_{tot} = \frac{\tau_{rad} + \tau_p}{\tau_{rad}\tau_p} \tag{12}$$

returning the Lorentzian lifetime broadening parameter, Γ,

$$\Gamma = \frac{1}{2\pi c\tau} \tag{13}$$

which is then substituted into the Voigt line profile along with the Doppler component. In principle, pressure effects can also be included in the Voigt profile, but here all results are for $P = 0$.

2.4 Photodissociation rates

The photodissociation rate, k, of a molecule dissociated by a field with flux dependent on wavelength $F(\lambda)$ through the photodissociation cross-sections $\sigma(\lambda; T)$ is given by equation (2). There are many

standard fluxes which are used to model different environments. In the recent ExoMol photodissociation cross-section release by Pezzella et al. (2022), the interstellar radiation field (ISRF), Solar radiation field, two models of the Proxima Centauri field, taken from PHOENIX (Husser et al. 2013) and MUSCLES (France et al. 2016; Loyd et al. 2016; Youngblood et al. 2016), and a blackbody radiation field (BB), $B(\lambda, T_{\rm rad})$, defined as,

$$B(\lambda, T_{\rm rad}) = \frac{2 \times 10^4}{4\pi\lambda^4} \frac{1}{e^{\frac{hc}{\lambda k_B T_{\rm rad}}} - 1}, \tag{14}$$

where k_B is the Boltzmann constant, h is Planck's constant, c is the speed of light, and $T_{\rm rad}$ is the temperature of the blackbody, were used to compute rates.

In this study the ISRF, BB, and Solar radiation fields will be used to produce temperature-dependent rates of OH for $T \in [300, 1000, 2000, 5000]$ K. OH is known to be photodissociatively active in interstellar clouds, especially through the $1\ ^2\Sigma^- \leftarrow X\ ^2\Pi$ band, which is the primary destructor of OH in this medium (van Dishoeck & Dalgarno 1983; Radenović et al. 2008). Also as OH is known to be present in sunspots (Berdyugina & Solanki 2001), BB and Solar flux modelling are sensible choices.

Other available OH photodissociation rates are largely computed using one or more of the first three radiation fields listed above (van Dishoeck & Dalgarno 1984b; Nee & Lee 1985). The Leiden data base (Hrodmarsson & van Dishoeck 2023) offers rates using the ISRF radiation field using the fit from Draine (1978), which is fit from 91.2 and 200 nm using the extension to higher wavelengths from van Dishoeck & Black (1982), the Solar radiation field compiled from the measurements of Woods et al. (1996) and Curdt et al. (2001), and blackbody radiation fields for $T_{\rm rad} \in [4000, 10000, 20000]$ K.

2.5 Short wavelength top-up

Paper II showed that the computed photoabsorption cross-section disagrees significantly with that of the Leiden data base (Hrodmarsson & van Dishoeck 2023) above 80 000 cm^{-1} ($\lambda < 125$ nm) as some high energy electronic states such as $2\ ^2\Pi$ and $3\ ^2\Pi$ were not included in our model. These states were not modelled as part of Paper II as experimental transitions are not available and *ab initio* electronic structure calculations proved unsuccessful due to complex avoided crossing structures. Omitting these states from the photodissociation cross-section calculation results in underestimated photodissociation rates for the ISRF, BB10K, and BB20K radiation fields as these flux distributions are relatively flat.

Since the calculated photodissociation cross-sections here are not suitable for rate calculations where $\lambda < 125$ nm is required, we truncate them to > 125 nm and substitute with the cross-sections from the Leiden data base for this region of the shorter wavelengths. While the Leiden spectra do not consider temperature, and so are somewhat incompatible with this data set for extension, temperature-dependent effects manifest themselves mainly at long wavelength, where our model is accurate. This top-up method is therefore deemed to be appropriate, however, it should be noted that the resultant cross-sections do not consider temperature effects for $\lambda < 125$ nm.

2.6 Non-LTE cross-sections

The calculations thus far are performed for a molecule assumed to be in local thermodynamic equilibrium (LTE), so that the populations of initial states follow a Boltzmann distribution. Many different processes including chemical reactions and photodissociation can result in products which are not in thermodynamic equilibrium. So in the cases where OH may be produced by such a process, the initial populations are not adequately characterized by the Boltzmann distribution. These lead to non-LTE spectral features where intensity is distributed rather differently, as populations are informed by the pre-requisite processes.

As such, the inclusion of non-LTE effects allows for more robust modelling of exoplanet atmospheric chemistry and chemical dynamics (Clark & Yurchenko 2021). In radiation-rich environments, such as those in exoplanets close to their mother star, where photodissociative processes are important (Pezzella et al. 2021), modelling non-LTE spectral features in photodissociation could be useful in detecting precursors of the dissociating molecule. One important example would be OH, whose non-LTE effects have been studied for their capacity for measuring the effective temperature of hot-Jupiter atmospheres (Wright et al. 2023). Moreover, OH is a dissociation product of water (Wang et al. 2017; Zannese et al. 2023), and in environments where an OH product is likely to dissociate prior to reaching thermal equilibrium, understanding its non-LTE photodissociation spectra can be useful not only in detecting OH, but also as an indirect tool for detecting water. These factors drive a need for cross-sections which are suitable for non-LTE studies where the populations of the initial states can be modified

The temperature-dependent intensity for a given transition in a thermalized molecule is given by,

$$I(f \leftarrow i, T) = \frac{g_f^{\rm tot} A_{fi}}{8\pi c \tilde{\nu}_{fi}^2} \cdot \frac{e^{-c_2 \tilde{E}_i/T} \left(1 - e^{-c_2 \tilde{\nu}_{fi}/T}\right)}{Q(T)}, \tag{15}$$

where f and i denote final and initial states respectively, $g_f^{\rm tot}$ is the total degeneracy of the final state, $\tilde{\nu}_{fi}$ is the line centre (in cm^{-1}), A_{fi} is the Einstein-A coefficient (s^{-1}), $\tilde{E}_i$ is the initial state energy term value (cm^{-1}), c_2 is the second radiation constant (K/cm^{-1}), T is the temperature (K), and $Q(T)$ is the partition function. This form assumes that initial populations are Boltzmann distributed with population, n_B:

$$n_B(T) = \frac{g_i^{\rm tot}}{Q(T)} e^{-c_2 \tilde{E}_i/T}. \tag{16}$$

Given this, one can rewrite equation (15) as,

$$I(f \leftarrow i, T) = \frac{n_B(T) g_f^{\rm tot} A_{fi}}{8\pi c \tilde{\nu}_{fi}^2 g_i^{\rm tot}} S(\tilde{\nu}_{fi}, T), \tag{17}$$

where $S(\tilde{\nu}_{fi}, T)$ is the self-absorption term. Except at high temperatures $S(\tilde{\nu}_{fi}, T)$ is close to unity at wavelengths relevant to photodissociation and it is neglected. Setting the thermal population n_B to unity, we define a temperature-independent, state-dependent line intensity (or absorption coefficient) for each state as

$$I(f \leftarrow i) = \frac{g_f^{\rm tot} A_{fi}}{8\pi c \tilde{\nu}_{fi}^2 g_i^{\rm tot}}. \tag{18}$$

Equation (18) is then used to produce separated cross-sections combining transitions for each relevant initial state, i, and summed over all possible final states, f, for a given the dissociation channel.

We thus provide cross-sections $\sigma(\lambda, i)$, for each initial state, i. These can then be used to form the population scaled (Non-LTE) cross-section $\sigma(\lambda)$ by summing all the contributions scaled with the associated lower state populations n_i. Computing cross-sections is computationally time consuming, especially for a fine grid spacing; so pre-computed cross-sections separated out by lower states with intensities independent of thermal effects give flexibility to the end

Table 1. Electronic bands of OH is included in the photodissociation spectrum and their associated dissociative properties.

Transition	Direct	Pre-dissociation	Smoothed (Direct)
$X\,^2\Pi \leftarrow X\,^2\Pi$			
$A\,^2\Sigma^+ \leftarrow X\,^2\Pi$	✓	✓	✓
$B\,^2\Sigma^+ \leftarrow X\,^2\Pi$	✓	✓	✓
$C\,^2\Sigma^+ \leftarrow X\,^2\Pi$		✓	
$1\,^2\Sigma^- \leftarrow X\,^2\Pi$	✓		✓
$1\,^2\Delta \leftarrow X\,^2\Pi$	✓		✓
$A\,^2\Sigma^+ \leftarrow A\,^2\Sigma^+$	✓	✓	
$B\,^2\Sigma^+ \leftarrow B\,^2\Sigma^+$	✓	✓	
$C\,^2\Sigma^+ \leftarrow C\,^2\Sigma^+$		✓	

user, as problem-specific populations can be used to produce full cross-sections at low cost.

It should be noted from equation (18) that our state-dependent cross-sections do not account for the self-absorption term seen in equation (15). The term should be reintroduced when combining the cross-sections, however, with the desired temperature/population distribution. As the temperature increases the effects of the self-absorption term, it becomes increasingly impactful at shorter wavelengths. The self-absorption term will always have a maximum effect at the low-wavelength end of the spectrum, i.e. at the 125 nm end. At low temperatures this is negligible, however scales poorly as temperature is increased; at 1000 K it gives rise to a less than a 1 per cent reduction in intensity and at 5000 K it accounts for a roughly 24 per cent reduction. At the 2000 nm end however, temperatures of roughly 25 000 K (i.e. above our limit) are required for the self-absorption term to account for even a 1 per cent reduction in intensity.

3 RESULTS

Temperature-dependent photodissociation cross-sections for the hydroxyl radical are produced in the range of $T \in [100, 10000]$ K in steps of 100 K on a wavelength grid of 0.1 nm ranging from 82.8 to 2000 nm. Table 1 summarizes the transitions which are included in the photodissociation spectrum of OH, and the types of transitions they are. Transitions which exhibit direct photodissociation or pre-dissociation are included in the photodissociation cross-sections.

Pre-dissociation cross-sections are calculated using PYEXOCROSS with a binned Voigt line profile (Zhang et al. 2024) and a non-uniform wavenumber grid such that upon conversion a uniform wavelength grid is recovered. Direct photodissociation cross-sections are similarly computed on a non-uniform wavenumber grid, with their Gaussian broadening parameters informed by the treatment in Section 2.2.

The resulting photodissociation cross-sections contain smoothed direct photodissociation cross-sections (Section 2.2) and unsmoothed, appropriately broadened pre-dissociation cross-sections (Section 2.3). Example cross-sections and a comparison with the available Leiden photodissociation cross-sections are given in Fig. 4. There is generally good agreement in the position of transition lines and cross-section intensity with the cross-section provided by the Leiden data base (Heays et al. 2017). However, the long wavelength cross-section is much sparser compared to our calculations which is likely due to an insufficient treatment of the pre-dissociative effects in the $A\,^2\Sigma^+$ state in Leiden data base cross-sections. Indeed, it appears that in the Leiden data base that the $A\,^2\Sigma^+$ state pre-dissociation intensity is concentrated entirely into the $A - X, v' = 2$ absorption band whereas we identify contributions from several bands. The cross-sections are available from the ExoMol photodissociation data base, ExoPhoto Ni et al. (2025), at www.exomol.com/exophoto/OH.

3.1 Non-LTE cross-sections

The spectroscopic model used here includes 2250 unique states in $X\,^2\Pi$ which comprise the set of initial states, $\{i\}$. Thus, for each dissociation channel, D, 2250 state-dependent cross-sections, $\sigma(\lambda; \mathrm{D}, i)$ are calculated and provided. For initial states which have no associated final states, cross-sections with all zeros are given for consistency. This data is given in the supplementary material as a .NLTE file with the format that the first column is the wavelength with column label *lambda* on a grid of 125 to 2000 nm with a 0.1 nm grid spacing.

The remaining columns have labels i_D, where i is the initial state, i and D is the dissociation channel for D = [A,S,D,B,C,T], where the labels correspond to the $A\,^2\Sigma^+$, $1\,^2\Sigma^-$, $D\,^2\Sigma^-$, $B\,^2\Sigma^+$, $C\,^2\Sigma^+$, upper state cross-sections, respectively, and T corresponds to the total cross-section. An extract of this data set is given in Table 2.

3.2 Rates

Photodissociation rates for OH can be calculated using the energy-dependent smoothed model of OH from Fig. 4 and the standard fluxes such as provided by the Leiden data base (Heays et al. 2017). The photodissociation cross-section of Leiden are complete down to 82 nm; as such the rate, $k_{82\,\mathrm{nm}}(T)$, can be evaluated using equation (2) with a lower limit λ_1 set to 82 nm and the upper limit λ_2 defined by the wavelength range of the given radiation field. To compare with the available literature rates, $k_{82\,\mathrm{nm}}(T = 1\ \mathrm{K})$ is calculated for various radiation fields; as Fig. 5 shows, good agreement is found. Rates agree closely with Leiden except for the BB4K radiation field. This is expected as BB4K is close to zero at ~ 125 nm and rises with wavelength. We believe our rates are correct as the cross-sections in the Leiden data base appear to be too low in $A\,^2\Sigma^+ \leftarrow X\,^2\Pi$ pre-dissociative region.

Temperature-dependent rates for $T \in [1, 300, 2000, 8000]$ K are presented in Fig. 6. Here we see the importance of not neglecting temperature effects when producing rates. In Fig. 5 we see an average rate difference of ~ 2.5 per cent when calculated at $T = 1$ K. When temperature effects are considered, however, we see that the photodissociation rates vary by orders of magnitude, especially for the 4000 K blackbody (BB4K) and Solar fluxes, where a three order of magnitude range is found. Modelling photodissociation in a hot environment with temperature independent cross-sections can therefore result in significantly underestimated photodissociation rates.

4 CONCLUSIONS AND FUTURE WORK

Energy-dependent smoothing is presented as a fast, easy to implement, and pragmatic method for producing temperature-dependent cross-sections, leveraging pre-existing DUO models. The photodissociation cross-sections and rates are in line with the available data from the Leiden data base (Heays et al. 2017). A rate roughly 30 per cent higher than that of Leiden is reported for the $B(\lambda, 4000\ \mathrm{K})$, a much higher photodissociation rate than previously expected, increasing dramatically with temperature. Due to the increased rate in this region, it is likely that these calculations would be particularly useful for studying OH photodissociation in sunspots and other similar main-sequence stars.

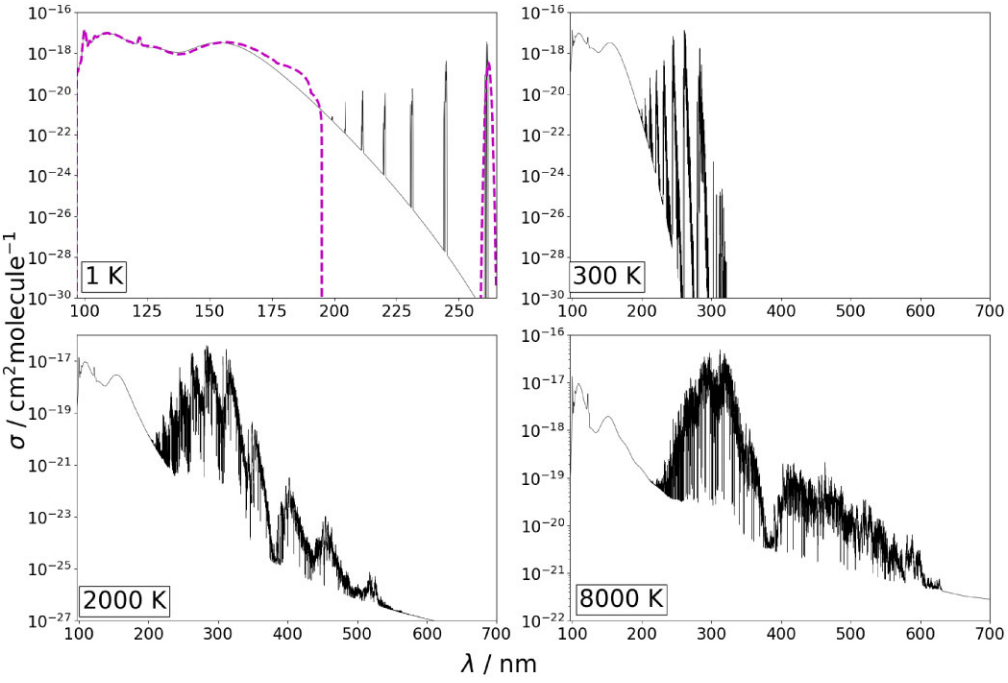

Figure 4. Photodissociation cross-section of OH at $T = 1, 300, 2000, 8000$ K. Solid lines are the energy-dependent smoothed cross-section, the dashed line in the top left panel is the Leiden data base cross-section (Heays, Bosman & van Dishoeck 2017). The panel for 1 K is plotted on a truncated wavelength grid to better show differences between our calculated cross-section and that of the literature.

Table 2. Extract of the OH .NLTE file containing non-LTE photodissociation cross-sections for 2250 initial states in X $^2\Pi$ as calculated using the methodology is 2.6. This is available in the supplementary material.

lambda	1_T	1_A	1_S	1_D	1_B	1_C	2_T	...
125.00	1.69818194E-18	6.00884347E-28	7.69257744E-21	1.62911998E-18	6.13693791E-20	0.00000000E + 00	1.66048939E-18	...
125.10	1.70431633E-18	6.10418458E-28	7.96601936E-21	1.63698878E-18	5.93615265E-20	0.00000000E + 00	1.65194727E-18	...
125.20	1.71021224E-18	6.20077117E-28	8.25059803E-21	1.64455500E-18	5.74066384E-20	0.00000000E + 00	1.64286351E-18	...
125.30	1.71582283E-18	6.29850747E-28	8.54676313E-21	1.65177767E-18	5.54983972E-20	0.00000000E + 00	1.63325500E-18	...
125.40	1.72111293E-18	6.39724060E-28	8.85493004E-21	1.65862201E-18	5.36359871E-20	0.00000000E + 00	1.62313196E-18	...
125.50	1.72607225E-18	6.49682231E-28	9.17548603E-21	1.66507309E-18	5.18236781E-20	0.00000000E + 00	1.61248882E-18	...
125.60	1.73071496E-18	6.59717052E-28	9.50881062E-21	1.67114061E-18	5.00655434E-20	0.00000000E + 00	1.60131253E-18	...
125.70	1.73506892E-18	6.69830544E-28	9.85530471E-21	1.67685293E-18	4.83606847E-20	0.00000000E + 00	1.58960261E-18	...
125.80	1.73916172E-18	6.80034502E-28	1.02154197E-20	1.68224275E-18	4.67035491E-20	0.00000000E + 00	1.57738677E-18	...
125.90	1.74300937E-18	6.90346041E-28	1.05896770E-20	1.68733095E-18	4.50887436E-20	0.00000000E + 00	1.56471671E-18	...

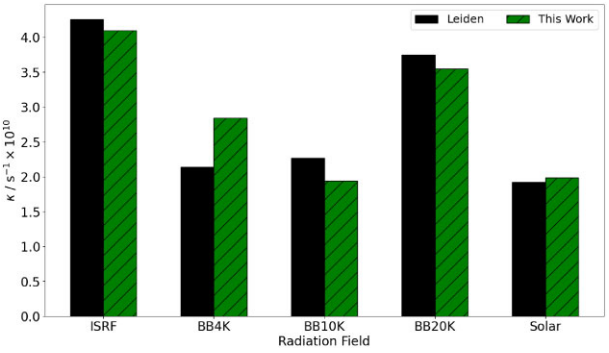

Figure 5. Comparison of photodissociation rates between those of Hrodmarsson & van Dishoeck (2023) and this work; our data are for a temperature of 1 K.

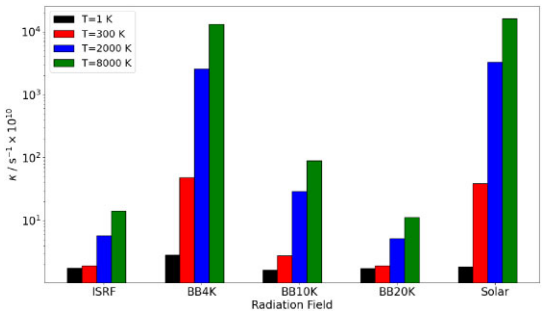

Figure 6. Our calculated temperature-dependent photodissociation rates of OH for various standard fluxes from Hrodmarsson & van Dishoeck (2023).

Furthermore, in diffuse, optically thin interstellar clouds, the primary channel for the destruction of OH through direct photodissociation is $1\ ^2\Sigma^- \leftarrow X\ ^2\Pi$, followed closely by $3\ ^2\Pi \leftarrow X\ ^2\Pi$ and $1\ ^2\Delta \leftarrow X\ ^2\Pi$, with relative rates in the ratio of $\sim 1 : 0.9 : 0.4$, respectively (van Dishoeck & Dalgarno 1983). The $1\ ^2\Sigma^- \leftarrow X\ ^2\Pi$ cross-section is of good quality, as the energy levels of $X\ ^2\Pi$ are experimental and the pre-dissociation lifetimes of $A\ ^2\Sigma^+$ presented in Papers I (Mitev et al. 2024) and II (Mitev et al. 2025) show good agreement with experiment. As the continuum states' curves have not been refined like those of the bound states, one can base their accuracy on the quality of the *ab initio* calculations. Additional evidence is given by the demonstrated accuracy of the $A\ ^2\Sigma^+$ state pre-dissociation lifetimes, which rely heavily on *ab initio* curves. These results indicate that it the theoretical curves should be sufficiently accurate for modelling continuum absorption cross-sections.

OH is a very complex dissociation prone molecule, with some sort of dissociative mechanism available for all excited electronic states. The notable exception to this is the small fully bound region in $A\ ^2\Sigma^+$ below $D_0(X)$. Photodissociation of the $A\ ^2\Sigma^+$ state in the region is not considered in this work but could be important, see Livingston Large & Kliewer (2024). Above the threshold to dissociation, all transitions are at least pre-dissociative or photodissociative. Some mechanisms that have not been considered fully here are rotational pre-dissociation, indirect pre-dissociation, and spontaneous radiative decay, the latter effect has been studied by Czarny et al. (1971), van der Loo & Groenenboom (2005), Greenslade et al. (2005), Heays et al. (2018) in the $D\ ^2\Sigma^-$ state and is a logical extension to studying dissociation dynamics of OH and extending the energy coverage of the cross-sections. The photodissociation of OD has also seen much study (van Dishoeck & Dalgarno 1984a; Nee & Lee 1984b, 1985; Radenović et al. 2003). Along with extending modelling to more dissociation mechanisms and including higher energy electronic states; including the OD and ^{18}OH isotopologues are sensible extensions. Further testing of energy-dependent smoothing is required and new implementations will be needed to extend treatment to polyatomics.

ACKNOWLEDGEMENTS

We acknowledge the use of the UCL Myriad High Performance Computing Facility (Myriad@UCL), and associated support services, in the completion of this work. This work was supported by ERC Advanced Investigator Project 883830 and by UK STFC under grant ST/Y001508/1.

DATA AVAILABILITY

Temperature-dependent photodissociation cross-sections for $T \in [100, 200, ..., 8000]$ K with a grid spacing of 0.1 nm are made available at www.exomol.com. The open access programs DUO, EXOCROSS, and PYEXOCROSS are available from github.com/exomol. State dependent cross-sections suitable for Non-LTE studies are available from the corresponding author on request.

REFERENCES

Berdyugina S. V., Solanki S. K., 2001, A&A, 380, L5
Bowesman C. A., Qu Q., McKemmish L. K., Yurchenko S. N., Tennyson J., 2024, MNRAS, 529, 1321
Brady R. P., Drury C., Yurchenko S. N., Tennyson J., 2024, J. Chem. Theory Comput., 20, 2127
Carr J. S., Najita J. R., 2014, ApJ, 788, 66
Chang Y. et al., 2019, Nat. Commun., 10, 1250
Chang Y. et al., 2020a, J. Phys. Chem. Lett., 11, 7617
Chang Y. et al., 2020b, J. Phys. Chem. Lett., 11, 9086
Cheng Y., Yuan K., Cheng L., Guo Q., Dai D., Yang X., 2011, J. Chem. Phys., 134, 064301
Clark V. H. J., Yurchenko S. N., 2021, Phys. Chem. Chem. Phys., 23, 11990
Curdt W., Brekke P., Feldman U., Wilhelm K., Dwivedi B. N., Schühle U., Lemaire P., 2001, A&A, 375, 591
Czarny J., Felenbok P., Lefebvre-Brion H., 1971, J. Phys. B-At. Mol. Opt. Phys., 4, 124
Dalgarno A., 1987, Int. J. Mass Spectr. Ion Process., 81, 1
Dixon R. N., Oliver T. A. A., Cheng L., Cheng Y., Yuan K., Yang X., 2013, J. Chem. Phys., 138, 104306
Draine B. T., 1978, ApJS, 36, 595
France K. et al., 2016, ApJ, 820, 89
Greenslade M. E., Lester M. I., Radenović D. C., van Roij A. J. A., Parker D. H., 2005, J. Chem. Phys., 123, 074309
Harich S. A., Yang Y. F., Yang X. M., 2001, Phys. Rev. Lett., 87, 253201
Heays A. N., Bosman A. D., van Dishoeck E. F., 2017, A&A, 602, A105
Heays A. N. et al., 2018, J. Quant. Spectrosc. Radiat. Transfer, 204, 12
Hrodmarsson H. R., van Dishoeck E. F., 2023, A&A, 675, A25
Huber P., Ronchetti E., 2009, Robust statistics. Wiley Series in Probability and Statistics. John Wiley, Hoboken
Husser T.-O., Wende-von Berg S., Dreizler S., Homeier D., Reiners A., Barman T., Hauschildt P. H., 2013, A&A, 553, A6
Hwang E. S., Lipson J. B., Field R. W., Dodd J. A., 2001, J. Phys. Chem. A, 105, 6030
Kalyanaraman C., Sathyamurthy N., 1994, Chem. Phys., 187, 219
Kurucz R. L., van Dishoeck E. F., Tarafdar S. P., 1987, ApJ, 322, 992
Li Y., Zhang P.-Y., 2011, J. Theor. Comp. Chem., 10, 747
Livingston Large T. A., Kliewer C. J., 2024, J. Chem. Phys., 160, 201102
Loyd R. O. P. et al., 2016, ApJ, 824, 102
Meinel I. A. B., 1950, ApJ, 111, 555
Mitev G. B., Yurchenko S. N., Tennyson J., 2024, J. Chem. Phys., 160, 144110
Mitev G. B., Bowesman C. A., Zhang J., Yurchenko S. N., Tennyson J., 2025, MNRAS, 536, 3401
Nee J. B., Lee L. C., 1984a, J. Chem. Phys., 81, 31
Nee J. B., Lee L. C., 1984b, J. Chem. Phys., 81, 3811
Nee J. B., Lee L. C., 1985, ApJ, 291, 202
Ni Q.-H., Hill C., Yurchenko S. N., Pezzella M., Fateev A. Z., Qin Z., Venot O., Tennyson J., 2025, RAS Tech. Instrum.,
Parkinson C. D., Bougher S. W., Mills F. P., Yung Y. L., Brecht A., Shields D., Liemohn M., 2021, Icarus, 368, 114580
Pezzella M., Yurchenko S. N., Tennyson J., 2021, Phys. Chem. Chem. Phys., 23, 16390
Pezzella M., Yurchenko S. N., Tennyson J., 2022, MNRAS, 514, 4413
Pezzella M., Mitev G., Yurchenko S. N., Tennyson J., Mitrushchenkov A. O., 2024, Phys. Chem. Chem. Phys., 26, 27519
Radenović D. Č. et al., 2003, J. Chem. Phys., 119, 9341
Radenović D. Č., van Roij A. J., Wu S.-M., Meulen J. T., Parker D. H., van der Loo M. P., Janssen L. M., Groenenboom G. C., 2008, Mol. Phys., 106, 557
Sappey A. D., Crosley D. R., Copeland R. A., 1989, J. Chem. Phys., 90, 3484
Schoerghofer N. et al., 2021, Space Sci. Rev., 217, 74
Sun G., Zheng X.-F., Qin Y., Song Y., Zhang J., Amero J. M., Vázquez G. J., 2020, Chinese J. Chem. Phys., 33, 129
Tabone B., van Hemert M. C., van Dishoeck E. F., Black J. H., 2021, A&A, 650, A192
Tabone B., van Dishoeck E. F., Black J. H., 2024, A&A, 691, A11
Tang N. et al., 2021, ApJS, 252, 1
Tappe A., Lada C. J., Black J. H., Muench A. A., 2008, ApJ, 680, L117
Tennyson J., Pezzella M., Zhang J., Yurchenko S. N., 2023, RAS Tech. Instrum., 2, 231
Uhlikova T., Yurchenko S. N., Perri A. N., Tennyson J., Kim G.-S., 2025, J. Chem. Phys., 162, 144108
van Dishoeck E. F., Black J. H., 1982, ApJ, 258, 533
van Dishoeck E. F., Dalgarno A., 1983, J. Chem. Phys., 79, 873

van Dishoeck E. F., Dalgarno A., 1984a, Icarus, 59, 305
van Dishoeck E. F., Dalgarno A., 1984b, ApJ, 277, 576
van Dishoeck E. F., van Hemert M. C., Allison A. C., Dalgarno A., 1984, J. Chem. Phys., 81, 5709
van der Loo M. P. J., Groenenboom G. C., 2005, J. Chem. Phys., 123, 074310
Wampfler S. F. et al., 2010, A&A, 521, L36
Wang Z. et al., 2017, AJ., 154, 249
Woods T. N. et al., 1996, J. Geophys. Res.-Atmos., 101, 9541
Wright S. O. M. et al., 2023, AJ, 166, 41
Youngblood A. et al., 2016, ApJ, 824, 101
Yuan K., Dixon R. N., Yang X., 2011, Acc. Chem. Res, 44, 369
Yurchenko S. N., Al-Refaie A. F., Tennyson J., 2018, A&A, 614, A131
Zannese M., Tabone B., Habart E., Le Petit F., van Dishoeck E. F., Bron E., 2023, A&A, 671, A41
Zhang J., Tennyson J., Yurchenko S. N., 2024, RAS Tech. Instrum., 3, 257
Zhu X., Yee J.-H., 2007, Icarus, 189, 136

This paper has been typeset from a TEX/LATEX file prepared by the author.